PHYSICAL REVIEW B VOLUME 45, NUMBER 4 15 JANUARY 1992-II

Rapid Communications

Rapid Communications are intended for the accelerated publication of important new results and are therefore given priority treatment both in the editorial office and in production. A Rapid Communication in **Physical Review B** *should be no longer than 4 printed pages and must be accompanied by an abstract. Page proofs are sent to authors.*

Oscillatory bistability of real-space transfer in semiconductor heterostructures

R. Döttling and E. Schöll

Institut für Theoretische Physik, Technische Universität Berlin, Hardenbergstrasse 36, D-1000 Berlin 12, Germany

(Received 31 May 1991; revised manuscript received 28 August 1991)

Charge transport parallel to the layers of a modulation-doped GaAs/$Al_xGa_{1-x}As$ heterostructure is studied theoretically. The heating of electrons by the applied electric field leads to real-space transfer of electrons from the GaAs into the adjacent $Al_xGa_{1-x}As$ layer. For sufficiently large dc bias, spontaneous periodic 100-GHz current oscillations, and bistability and hysteretic switching transitions between oscillatory and stationary states are predicted. We present a detailed investigation of complex bifurcation scenarios as a function of the bias voltage U_0 and the load resistance R_L. For large R_L subcritical Hopf bifurcations and global bifurcations of limit cycles are displayed.

In this paper we consider parallel transport in a modulation-doped GaAs/$Al_xGa_{1-x}As$ heterostructure as schematically shown in Fig. 1(a). The $Al_xGa_{1-x}As$ layer is heavily n-type doped with donor density N_D, while the GaAs layer is undoped. At low bias U_0 the electrons reside in the GaAs channel, where they are separated from their parent donors in the $Al_xGa_{1-x}As$ layer. Thus the mobility μ_1 of the electrons in the GaAs layer is high because of the reduced impurity scattering. An electric field parallel to the layer interface induces carrier heating. If the electrons gain enough kinetic energy, thermionic emission across the barrier [Fig. 1(b)] into the $Al_xGa_{1-x}As$ layer is possible, where the mobility μ_2 is much lower due to impurity scattering. This real-space transfer of electrons from the high-mobility to the low-mobility layer causes an N-shaped current-voltage characteristic with a regime of negative differential conductivity[1-7] (NNDC) in analogy with intervalley transfer in the Gunn effect.

In the NNDC regime, ac-driven current oscillations of 2–25 MHz have been reported.[8] Oscillations in heterolayers were also observed under dc conditions.[9,10] A physical mechanism of a real-space transfer oscillator, which gives periodic[11] and chaotic[6,12] self-generated oscillations at much *higher* frequencies (20–80 GHz) under dc *conditions,* has recently been proposed and numerically investigated.[11] It is based on the coupled nonlinear dynamics of the real-space electron transfer and of the space charge in the $Al_xGa_{1-x}As$ layer, which controls the interface potential barrier Φ_B [Fig. 1(b)]. Real-space transfer of the electrons in the GaAs layer leads to an increase of the carrier density in the $Al_xGa_{1-x}As$, which diminishes the positive space charge controlling the band bending. Subsequently, the potential barrier Φ_B decreases with some delay due to the finite dielectric relaxation time. This leads to an increased backward thermionic emission current which decreases the carrier density in the $Al_xGa_{1-x}As$. Hence the space charge and Φ_B are increased. This, in turn, decreases the backward thermionic emission current, which completes the cycle.

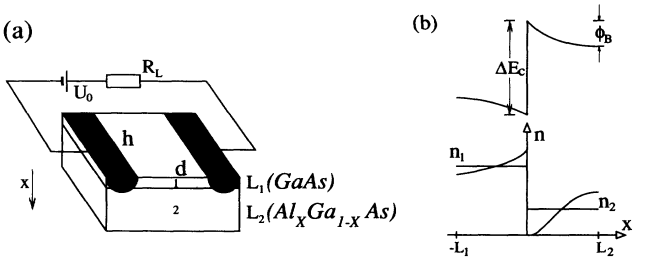

FIG. 1. (a) Schematic sample and circuit configuration of a modulation-doped GaAs/$Al_xGa_{1-x}As$ heterostructure with heterolayer width L_1 and L_2, respectively, and lateral dimensions h, d. (b) Energy-band diagram (top) and carrier density (bottom) vs the perpendicular coordinate x of the heterolayer (schematic).

In the present paper we show that real-space transfer can also lead to S-shaped static current-bias voltage characteristics (SNDC) if the external circuit conditions are chosen appropriately, and that bistability between stationary and oscillatory states is then possible. We investigate in detail the resulting bifurcation scenarios as a function of bias voltage U_0 and load resistance R_L. Similar methods of nonlinear dynamics have recently been applied to a different oscillation mechanism in bulk semiconductors.[13]

In the following we derive a reduced set of nonlinear differential equations for the carrier densities n_1, n_2 in the two layers, the dielectric relaxation of the applied field $\mathcal{E}_\parallel$, and the potential barrier Φ_B.

The spatially averaged carrier density in the GaAs layer $n_1 \equiv \int_{-L_1}^{0} n(x,t)dx/L_1$, as a function of time, is governed

by the equation of continuity

$$\dot{n}_1 = \frac{1}{eL_1}(J_{1\to 2} - J_{2\to 1}), \tag{1}$$

where

$$J_{1\cdot 2} \equiv -en_1\left(\frac{E_1}{3\pi m_1^*}\right)^{1/2}\exp\left(-\frac{3\Delta E_c}{2E_1}\right),$$

$$J_{2\cdot 1} \equiv -en_2\left(\frac{E_2}{3\pi m_2^*}\right)^{1/2}\exp\left(-\frac{3\Phi_B}{2E_2}\right)$$

are the thermionic-emission-current densities (m_i^* are the effective masses) given by Bethe's theory,[14] and $E_i = \frac{3}{2}k_B T_i$ ($i=1,2$) are the mean carrier energies given by the carrier temperatures T_i. The thermionic emission theory corresponds to the following physical picture. Electrons in the GaAs with energy less than ΔE_c cannot propagate into the adjacent $Al_xGa_{1-x}As$ layer; all electrons with higher energy are emitted across the barrier without collisions. This is correct only within a certain region that is of the order of the mean free path of electrons. If the GaAs/$Al_xGa_{1-x}As$ layers are wider, the thermionic emission current represents the current only close to the interface, and diffusive currents play a major role. Intervalley transfer has been shown[15] to be negligible compared to real-space transfer at electric fields $\mathcal{E}_\parallel^* \leq 4$ kV/cm, as used here. Quantum effects like the quantum-transmission coefficient or tunneling through the barrier are also disregarded, cf. discussion in Ref. 16. Size-quantization effects, which arise if the layer widths are smaller than 100 Å, are also neglected, since the current-voltage characteristic is not essentially affected by the quasi-two-dimensional subbands below the barrier, except that the critical field for the onset of real-space transfer is shifted to higher values.[3]

Conservation of the total number of carriers requires $n_1L_1 + n_2L_2 = N_D L_2$, with $n_2 \equiv \int_0^{L_2} n(x,t)dx/L_2$.

The energy transfer between the heterolayers is described by the energy-balance equations containing Joule's heat, convective, diffusive, and electron-pressure-induced heat flow, and energy loss due to polar-optical-phonon scattering.[6] It can be shown by a linear mode analysis[17] that for reasonable numerical parameters the energy relaxation occurs on a fast time scale, such that E_1 and E_2, respectively, can be eliminated adiabatically from the energy-balance equations. The mean energy as a function of the applied electric field $\mathcal{E}_\parallel$ is then roughly estimated by

$$E_1 \approx E_L + \tau_E e\mu_1 \mathcal{E}_\parallel^2, \quad E_2 \approx E_L,$$

with the lattice energy $E_L = \frac{3}{2}k_B T_L$ and the energy relaxation time τ_E. This simplified approach is sufficient to gain physical insight into the mechanism of real-space transfer-induced oscillations.

The dielectric relaxation of the parallel electric field is given by

$$\epsilon\dot{\mathcal{E}}_\parallel = -\sigma_L(\mathcal{E}_\parallel - \mathcal{E}_0) - \frac{en_1\mu_1L_1 + en_2\mu_2L_2}{L_1+L_2}\mathcal{E}_\parallel, \tag{2}$$

where ϵ is the permittivity, $\sigma_L = [h(L_1+L_2)R_L/d]^{-1}$ is connected to the load resistance R_L, and $U_0 = \mathcal{E}_0 d$ is the applied bias voltage.

The interface potential barrier $\Phi_B \equiv -e\int_0^{L_2}\mathcal{E}_\perp(x,t)dx$ is governed by the space-charge dynamics in the $Al_xGa_{1-x}As$ layer and the resulting internal electric field $\mathcal{E}_\perp$. As shown in Ref. 11, the dynamics of Φ_B is given by

$$\dot{\Phi}_B = \frac{e}{\epsilon}\left(-\mu_2 N_D \Phi_B + \mu_2\frac{e^2}{2\epsilon}L_1^2 n_1^2 - eL_1L_2\dot{n}_1\right), \tag{3}$$

where we have neglected the diffusive contributions, which is appropriate if L_2 is less or comparable to the mean free path of the electrons.

The autonomous nonlinear dynamic system [Eqs. (1)–(3)], which is a reduction of the five-variable system treated in Ref. 11, constitutes the basis of our analysis.

The static current-density-field characteristic resulting from Eqs. (1)–(3) is shown in Fig. 2(a). Real-space transfer of hot electrons leads to NNDC. The intersection of the load line with the device characteristic defines the steady-state operating points. As the applied voltage U_0 is varied, the load line is shifted parallel and the intersection points move along the current-density-field characteristic. When the load line becomes tangential to the characteristic ($U_0 = U_{\rm th}$ or U_h), two intersection points merge at $\mathcal{E}_{{\rm sn}_1}^*$ and $\mathcal{E}_{{\rm sn}_2}^*$, respectively, and disappear upon further variation of U_0. In Fig. 2(b) the current is plotted versus the control parameter U_0, exhibiting inverted SNDC.

The stability of the steady state (denoted by an asterisk) $\underline{q}^* \equiv (n_1^*, \mathcal{E}_\parallel^*, \Phi_B^*)^T$ against infinitesimal fluctuations $\delta\underline{q}(t) = \delta\underline{q}(0)e^{\lambda t}$ is determined by linearizing the dynamical system (1)–(3) around its steady state and computing the eigenvalues λ of the Jacobian matrix $J(\underline{q}^*)_{ij} = (\partial\dot{q}_i/\partial q_j)^*$, $i,j=1,2,3$. Figure 3 shows the eigenvalues as a function of the static electric field $\mathcal{E}_\parallel^*$, which is related to the control parameter U_0 by (2), taken in the steady state. The third eigenvalue is always negative ($\lambda_3 < 0$, $|\lambda_3| \gg 1$) and is not shown; it is associated with $\mathcal{E}_\parallel$, which is therefore a fast dynamic variable and can be eliminated adiabatically. The resulting two-variable system (marked with a tilde) has eigenvalues $\tilde{\lambda}$, which are topologically equivalent to those in Fig. 3, but more amenable to

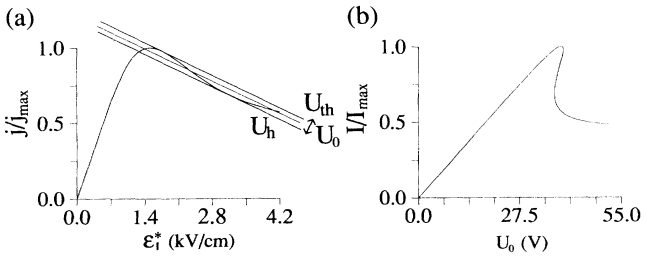

FIG. 2. (a) Static current-density-field characteristic as a function of the static electric field $\mathcal{E}_\parallel^*$. The load line is shown for three different bias voltages U_0. (b) Normalized current vs U_0. [The numerical parameters are $N_D = 10^{17}$ cm^{-3}, $L_1 = 100$ Å, $L_2 = 200$ Å, $\mu_1 = 8000$ cm^2/Vs, $\mu_2 = 50$ cm^2/Vs, $T_L = 300$ K, $\Delta E_c = 250$ meV ($x=0.3$), $m_1^* = 0.067m_0$ (m_0 is the free-electron mass), $m_2^* = (0.067+0.083x)m_0$, $\tau_E = 5.0\times10^{-12}$ s, $h = 1$ mm, $d = 50$ μm, $\epsilon = 12\epsilon_0$ (ϵ_0 is the vacuum permittivity), $R_L = 1.144$ kΩ.]

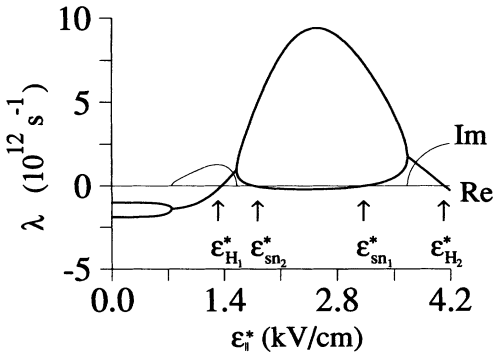

FIG. 3. Eigenvalue spectrum λ as a function of $\mathcal{E}_\parallel^*$. Bold and thin lines represent the real and imaginary parts of λ, respectively. $\mathcal{E}^*_{H_1}$, $\mathcal{E}^*_{H_2}$ mark Hopf bifurcations and $\mathcal{E}^*_{sn_1}$, $\mathcal{E}^*_{sn_2}$ mark saddle-node bifurcations. (Parameters as in Fig. 2.)

analytical treatment.

Let us now discuss the occurring bifurcations of the steady state $\underline{q}^*$ in the phase space $(n_1, \mathcal{E}_\parallel, \Phi_B)^T$. Upon increasing $\mathcal{E}_\parallel^*$, a stable node (three real negative eigenvalues) turns into a stable focus, which becomes unstable via a Hopf bifurcation at $\mathcal{E}^*_{H_1}$ (i.e., a pair of complex conjugate eigenvalues obtains positive real parts). The unstable saddle focus is transformed into a saddle point with two positive and one negative eigenvalues, and merges at $\mathcal{E}^*_{sn_2}$ with a saddlepoint with one positive and two negative eigenvalues, corresponding to the turning point U_{th} of the $I(U_0)$ characteristic (Fig. 2). A reverse bifurcation scenario $(\mathcal{E}^*_{sn_1}, \mathcal{E}^*_{H_2})$ takes place upon further increase of $\mathcal{E}_\parallel^*$, corresponding to the lower branch of Fig. 2(b).

The numerical simulation of the time-dependent nonlinear equations (1)–(3) reveals a more complex bifurcation scenario as a result of global bifurcations of limit cycles by condensation of paths or from a separatrix.[18,19] These supplement the local bifurcations shown in Fig. 3. Figure 4 summarizes schematically the global and local bifurcations (1–10). The bold lines denote stable fixed points (steady states) or limit cycles (periodic oscillations). On passing through the bifurcation value $\mathcal{E}_{c_1}$ (2), a stable and an unstable limit cycle are created from condensation of paths. The unstable limit cycle (dotted line) shrinks and collides at $\mathcal{E}_{ho_1}$ (3) with the saddlepoint (*SA*) (dashed line). A saddle-to-saddle separatrix loop (homoclinic orbit) is formed surrounding the fixed points on the upper and lower branch. Upon increase of $\mathcal{E}_0$, the separatrix disappears. At $\mathcal{E}_{ho_2}$ (4), a homoclinic orbit around the fixed point on the lower branch is formed, from which a limit cycle $\underline{q}(t)$ bifurcates. The stability of this periodic orbit $\tilde{\underline{q}}(t)$ in the reduced two-variable system is given in a linear approximation by the Floquet exponent γ_{lc}:[20]

$$\gamma_{lc} = (1/T)\int_{-T/2}^{T/2} \mathrm{Tr}\underline{\tilde{J}}[\tilde{\underline{q}}(t')]dt',$$

where Tr denotes the trace, and T is the oscillation period. γ_{lc} is a generalization of the eigenvalues of the Jacobian matrix controlling the stability of *fixed points*. In the limit $\tilde{\mathcal{E}} \to \tilde{\mathcal{E}}_{ho_2}$, the limit cycle collides with the saddle $\tilde{\underline{q}}^*$ of the middle branch. This yields $\gamma_{lc} = \mathrm{Tr}\underline{\tilde{J}}(\tilde{\underline{q}}^*) > 0$, which means that the homoclinic orbit and the bifurcating limit cycle are unstable. The unstable cycle appears immediately with a nonzero amplitude, but with zero frequency.

Upon further increase of $\mathcal{E}_0$, the unstable limit cycle shrinks and disappears via a subcritical Hopf bifurcation at $\mathcal{E}_{H_1}$ (5). When $\mathcal{E}_0$ passes $\mathcal{E}_{H_2}$ (6), an unstable limit cycle is created from a focus. As $\mathcal{E}_0$ increases, this unstable cycle expands and collides at $\mathcal{E}_{ho_3}$ (7) with the saddle point (*SA*), and a saddle-to-saddle loop is formed around the fixed point on the upper branch. At the bifurcation value $\mathcal{E}_{ho_4}$ (8), another homoclinic orbit surrounding both fixed points on the upper and lower branches is created, from which an unstable limit cycle bifurcates. After that, the unstable cycle expands and coalesces at $\mathcal{E}_{c_2}$ (9) with the stable limit cycle. In this way, a stable limit cycle is annihilated by a collision with an unstable cycle, forming a semistable limit cycle with multiplicity[21] 2 at $\mathcal{E}_{c_2}$.

We shall now discuss the physical implications. As the bias $\mathcal{E}_0$ is increased, the steady state (*SF*) becomes unstable at $\mathcal{E}_{H_1}$ (5), and finite-amplitude current and voltage

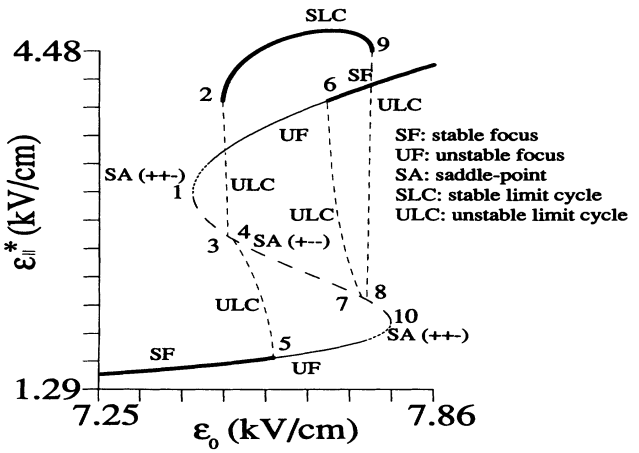

FIG. 4. Bifurcation diagram of the static electric field $\mathcal{E}_\parallel^*$ vs the control parameter $\mathcal{E}_0 = U_0/d$. The local and global bifurcations are denoted by 1–10; see text. (Parameters as in Fig. 2.)

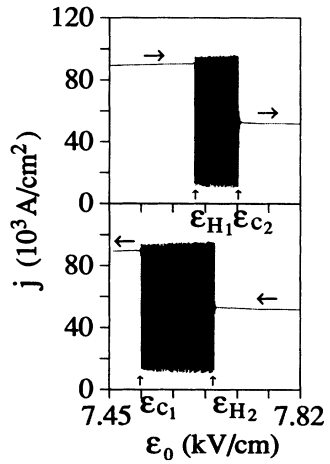

FIG. 5. Hysteresis of oscillatory (shaded) and stationary states. The time-dependent current density is plotted vs the applied field $\mathcal{E}_0$ for slowly increasing (top) and slowly decreasing (bottom) $\mathcal{E}_0$. The oscillation frequency is $f = 103$ GHz. (Parameters as in Fig. 2.)

oscillations set on, corresponding to the stable limit cycle (SLC) in the space of the dynamic variables $(n_1, \mathcal{E}_\parallel, \Phi_B)^T$. The drifting carriers cycle periodically between the GaAs and the $Al_xGa_{1-x}As$ layer, with a concomitant variation of the drift field $\mathcal{E}_\parallel$ and the potential barrier Φ_B. Note that this occurs in the *positive* differential conductivity regime. Upon further increase of $\mathcal{E}_0$, the oscillations cease at $\mathcal{E}_{c_2}$ (9), and the steady state (*SF*) on the other branch takes over (Fig. 5, top). When $\mathcal{E}_0$ is decreased, this steady state persists until $\mathcal{E}_{H_2}$ (6) $< \mathcal{E}_{c_2}$, where finite-amplitude oscillations set on, ceasing at $\mathcal{E}_{c_1}$ (2) $< \mathcal{E}_{H_1}$, and thus exhibiting dynamic hysteresis (Fig. 5, bottom).

Figure 6 shows the coexistence of two attractors (a stable limit cycle and a stable focus *SF*) in the hysteretic regimes $\mathcal{E}_{ho_2} < \mathcal{E}_0 < \mathcal{E}_{H_1}$ and $\mathcal{E}_{H_2} < \mathcal{E}_0 < \mathcal{E}_{ho_3}$. The two corresponding basins of attraction are separated by an unstable limit cycle (dashed line). The motion along the stable limit cycle (bold line) is clockwise.

For smaller load resistance R_L, the path condensation of limit cycles [(2) and (9) in Fig. 4] can occur beyond the multistationary regime. The generated semistable limit cycle decomposes into a stable and an unstable limit cycle; the latter shrinks upon variation of the control parameter and vanishes via a subcritical Hopf bifurcation. Thus there are no homoclinic bifurcations in this scenario.

If R_L is so small that $\sigma_L + \sigma_{\text{diff}} > 0$ throughout, where $\sigma_{\text{diff}} = dj/d\mathcal{E}_\parallel$ is the differential conductance, multistationarity (SNDC) does not occur, but bistability between limit cycles and the stationary state is still possible.

In conclusion, we have predicted complex bifurcation scenarios of self-oscillatory and stationary states for parallel transport in a modulation-doped heterostructure. The oscillation mechanism is based upon the delayed feedback between the thermionic emission current across the layer interface and the resulting space-charge dynamics of the potential barrier. A previous five-variable model[11,12] has been reduced to a nonlinear dynamic system with the averaged carrier density in the GaAs layer and the space-charge potential barrier in the $Al_xGa_{1-x}As$ layer as the essential variables. We have investigated the influence of the circuit conditions on the onset of the oscillations, and have demonstrated the possibility of oscillatory instabilities for sufficiently large load resistance in regimes of positive differential conductivity via a global bifurcation of a limit cycle. Further, subcritical Hopf bifurcations, the bifurcation of an unstable limit cycle from a homoclinic orbit, and, in particular, bistability and hysteretic switching between oscillatory and stationary states are found.

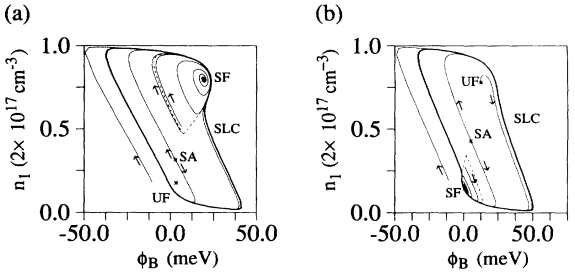

FIG. 6. Coexistence of two stable attractors. Phase portraits of n_1 vs Φ_B for (a) $\mathcal{E}_{ho_2} < \mathcal{E}_0 < \mathcal{E}_{H_1}$ and (b) $\mathcal{E}_{H_2} < \mathcal{E}_0 < \mathcal{E}_{ho_3}$. [Parameters as in Fig. 2 with (a) $\mathcal{E}_0 = 7.497$ kV/cm and (b) $\mathcal{E}_0 = 7.7006$ kV/cm].

Helpful discussions with K. Aoki, M. Asche, J. Kolodzey, M. Mocker, and P. Vogl are acknowledged.

[1] Z. S. Gribnikov, Fiz. Tekh. Poluprovodn. **6**, 1380 (1972) [Sov. Phys. Semicond. **6**, 1204 (1973)].

[2] F. Pacha and F. Paschke, Electron. Commun. **32**, 235 (1978).

[3] K. Hess, H. Morkoc, H. Shichijo, and B. G. Streetman, Appl. Phys. Lett. **35**, 469 (1979).

[4] H. Shichijo, K. Hess, and B. G. Streetman, Solid-State Electron. **23**, 817 (1980).

[5] R. Sakamoto, K. Akai, and M. Inoue, IEEE Trans. Electron Devices **36**, 2344 (1989).

[6] K. Aoki, K. Yamamoto, N. Mugibayashi, and E. Schöll, Solid-State Electron. **32**, 1149 (1989).

[7] A. Kastalsky, M. Milshtein, L. G. Shantharama, J. Harbison, and L. Florez, Solid-State Electron. **32**, 1841 (1989).

[8] P. D. Coleman, J. Freeman, H. Morkoc, K. Hess, B. G. Streetman, and M. Keever, Appl. Phys. Lett. **40**, 493 (1982).

[9] A. J. Vickers, A. Straw, and J. S. Roberts, Semicond. Sci. Technol. **4**, 743 (1989).

[10] P. Hendriks, E. A. E. Zwaal, J. G. A. Dubois, F. A. P. Blom, and J. H. Wolter, J. Appl. Phys. **69**, 302 (1991).

[11] E. Schöll and K. Aoki, Appl. Phys. Lett. **58**, 1277 (1991).

[12] E. Schöll and K. Aoki, in *Proceedings of the Twentieth International Conference on the Physics of Semiconductors*, edited by E. H. Anastassakis and J. D. Joannopoulos (World Scientific, Singapore, 1990), p. 1125.

[13] G. Hüpper and E. Schöll, Phys. Rev. Lett. **66**, 2372 (1991).

[14] K. Hess, *Advanced Theory of Semiconductor Devices* (Prentice-Hall, Englewood Cliffs, NJ, 1988).

[15] K. F. Brennan and D. H. Park, J. Appl. Phys. **65**, 1156 (1989).

[16] T. H. Glisson, J. R. Hauser, M. A. Littlejohn, K. Hess, B. G. Streetman, and H. Shichijo, J. Appl. Phys. **51**, 5445 (1980).

[17] D. Reznik (unpublished).

[18] E. Schöll, *Nonequilibrium Phase Transitions in Semiconductors* (Springer, Berlin, 1987).

[19] J. Guckenheimer and P. Holmes, *Nonlinear Oscillations, Dynamical Systems, and Bifurcations of Vector Fields*, Applied Mathematical Sciences Vol. 42 (Springer, New York, 1983).

[20] S. N. Chow and J. K. Hale, *Methods of Bifurcation Theory* (Springer, Berlin, 1982).

[21] A. A. Andronov, E. A. Leontovich, I. I. Gordon, and A. G. Maier, *Theory of Bifurcations of Dynamic Systems on a Plane* (Israel Program for Scientific Translations, Jerusalem, 1971), Vol. 2.

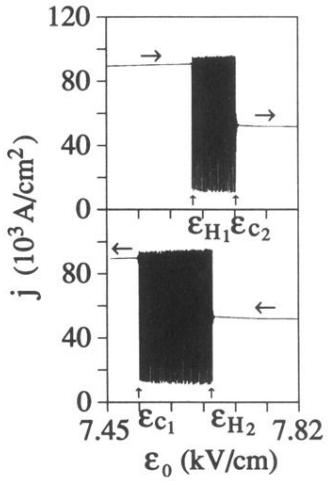

FIG. 5. Hysteresis of oscillatory (shaded) and stationary states. The time-dependent current density is plotted vs the applied field $\mathcal{E}_0$ for slowly increasing (top) and slowly decreasing (bottom) $\mathcal{E}_0$. The oscillation frequency is $f=103$ GHz. (Parameters as in Fig. 2.)